ELSEVIER

Computational Geometry 19 (2001) 175–189

Computational Geometry
Theory and Applications

www.elsevier.com/locate/comgeo

Delaunay conforming iso-surface, skeleton extraction and noise removal

D. Attali [a,*], J.-O. Lachaud [b]

[a] *LIS laboratory, Domaine Universitaire, BP 46, 38402 Saint-Martin d'Hères, France*
[b] *LaBRI laboratory, Domaine Universitaire, 351 Cours de la Liberation, 33405 Talence, France*

Communicated by M. Bern; received 23 June 2000; received in revised form 12 January 2001

Abstract

Iso-surfaces are routinely used for the visualization of volumetric structures. Further processing (such as quantitative analysis, morphometric measurements, shape description) requires volume representations. The skeleton representation matches these requirements by providing a concise description of the object. This paper has two parts. First, we exhibit an algorithm which locally builds an iso-surface with two significant properties: it is a 2-manifold and the surface is a subcomplex of the Delaunay tetrahedrization of its vertices. Secondly, because of the latter property, the skeleton can in turn be computed from the dual of the Delaunay tetrahedrization of the iso-surface vertices. The skeleton representation, although informative, is very sensitive to noise. This is why we associate a graph to each skeleton for two purposes: (i) the amount of noise can be identified and quantified on the graph and (ii) the selection of the graph subpart that does not correspond to noise induces a filtering on the skeleton. Finally, we show some results on synthetic and medical images. An application, measuring the thickness of objects (heart ventricles, bone samples) is also presented.

Keywords: Volumetric imaging; Iso-surface; Delaunay tetrahedrization; Voronoi graph; Skeleton

1. Introduction

Volumetric image analysis often requires, as a first step, the computation and display of surfaces which approximate the object boundaries. *Iso-surfaces* are perhaps the simplest surfaces that can be derived from volumetric images. Iso-surface approximations are constructed over vertices which lie in the 3-dimensional Euclidean space. As a set of triangles, iso-surfaces are easy to display. Furthermore, they can be extracted very efficiently from volumetric images.

Unfortunately, iso-surfaces provide a *surface representation* of objects, which might be inadequate in a context other than visualization. The analysis of volumetric images requires the extraction of structural information on objects. Other representations describing the inner part of objects are therefore necessary:

* Corresponding author.
E-mail addresses: Dominique.Attali@inpg.fr (D. Attali), lachaud@labri.u-bordeaux.fr (J.-O. Lachaud).

0925-7721/01/$ – see front matter
PII: S0925-7721(01)00019-0

- The *skeleton* is one of them. The skeleton describes objects by their axis of symmetry. It provides a concise inner representation of objects appropriate for image analysis. The skeleton can be used to extract various features such as the object thickness, as illustrated in Section 4.
- A *mesh decomposition* of the inner part of objects provides another example of a volume representation of objects. The object is represented by a set of cells (tetrahedra or cubes) glued together along their faces. This representation is suited to various applications, including physical modeling by finite elements.

Extracting volume representations from surface representations is generally not obvious. For triangulated surfaces, the work is greatly simplified if the surface is included in the Delaunay tetrahedrization of its vertices. Surfaces satisfying this property are said to be *Delaunay conforming*. The skeleton can then be deduced from the Voronoi graph of the surface vertices and the object can be decomposed into Delaunay tetrahedra.

Different approaches have been proposed to constrain surfaces. One approach refines surfaces, by adding points until every boundary triangles are forced into the Delaunay triangulation [10,26]. Some reconstruction methods produce directly Delaunay conforming surfaces [2,6,11].

In this paper, we use the fact that we are considering iso-surfaces. Therefore, we propose a different approach. We build iso-surfaces that are directly included in the Delaunay tetrahedrization of their vertices. The proposed method is performed locally and remains valid, whatever is the size of volume elements. Existing methods do not guarantee such a geometrical property. Our contribution is to build iso-surfaces that are Delaunay conforming. We also prove that the constructed surface is a 2-manifold.

This construction allows us to derive the skeleton of objects, along with a volume representation. This leads us to the second part of this paper, which focuses on the skeleton computation and filtering. A well-known drawback of the skeleton transformation is its lack of continuity. Noise on the boundary of an object may significantly change the aspect of its skeleton. A simplification algorithm is therefore necessary to remove peripheral branches having no perceptual relevance.

Existing methods left unresolved some crucial aspect of the simplification problem. They do not study the effect of noise on the skeleton. They depend on thresholds that are difficult to find automatically as they change with the objects. In this paper, three questions are raised and tackled:

(1) *What type of noise may affect real objects*? A model of noise is proposed that turns out to be realistic for a large amount of objects.
(2) *What is the influence of this type of noise on the skeleton*? The effect of noise on the skeleton is studied and a characterization of noisy branches is deduced.
(3) *How to select thresholds for simplification*? A graph is introduced on which thresholds for simplification can easily be selected.

Paper overview. The first part of this paper (Section 2) is devoted to the construction of Delaunay conforming iso-surfaces. The second part (Section 3) focuses on skeleton computation and filtering. Finally, in Section 4, some results on volumetric images are presented and an application to the thickness computation of objects is described.

Notations. Let $\mathbb{Z}$ be the set of integers and $\mathbb{R}$ be the set of real numbers. $\mathbb{Z}^d$ is the discrete d-dimensional space and $\mathbb{R}^d$ the Euclidean d-dimensional space. Let $V \subset \mathbb{R}^d$ be a set of n points. $\mathrm{Del}(V)$ denotes the Delaunay tetrahedrization of V, $\mathrm{Vor}(V)$ denotes the Voronoi graph of V and $\mathrm{Hull}(V)$ denotes the convex

hull of V, i.e., the smallest convex set in $\mathbb{R}^d$ containing V. The boundary of any subset A of $\mathbb{R}^3$ is denoted by ∂A (∂A is the closure of the set A minus its interior points).

2. Delaunay conforming iso-surfaces

2.1. Image iso-surfaces and classical approximation method

A gray-level *volumetric image* $\mathcal{I}$ is a mapping from a set $U \subset \mathbb{Z}^3$ onto the set of real numbers $\mathbb{R}$. Each element of U is called a *voxel*. The image $\mathcal{I}$ may be viewed as a sampling of a scalar continuous field h on the vertices of this discrete grid. The set of points where h takes the value C defines a *surface* $\mathcal{S}_C$ (i.e., $\mathcal{S}_C = \{M \in \mathbb{R}^3,\ h(M) = C\}$). In the following, we use the term "iso-surface" for any triangulated surface that approaches $\mathcal{S}_C$. We assume the image $\mathcal{I}$ is finite and its border is composed of only outer voxels or of only inner voxels.

The most common method for computing iso-surfaces in images is certainly the *marching-cubes* (MC) algorithm [21]. Its principle is to analyze the image locally using blocks of eight mutually adjacent voxels. These blocks are called *8-cubes*. Within each 8-cube, a set of triangles is found which separates *inner voxels* ($h(v) \geqslant C$) from *outer voxels* ($h(v) < C$). A *C-vertex* of the iso-surface is defined as a point lying on a grid edge between adjacent, inner and outer, voxels. A linear interpolation model is used to estimate where the iso-surface intersects this edge and determine an appropriate position for the C-vertex. Different sets of triangles may be constructed on the set of C-vertices of an 8-cube. The chosen triangulation influences the geometry and the topology of the iso-surface, and hence the properties of the approximation.

The MC algorithm exhibits an arbitrary choice, which depends only on the inner or outer classification of the 8-cube voxels. The vector gathering the classification ("inner" or "outer") of the voxels of an 8-cube is called a *configuration*. There are 256 different configurations. This leads to 256 possible triangulations within an 8-cube. The MC algorithm optimizes the running time of surface construction by pre-computing a table associating each configuration to a triangulation. Some authors refine this choice by using different kinds of interpolation or by exploiting gradient information (see [13] for a survey). However, none of these methods consider the geometry of the C-vertices, which explains why the computed iso-surface does not, in general, coincide with the Delaunay tetrahedrization.

2.2. Proposed method for building iso-surfaces

To build a triangulated iso-surface that is included in the Delaunay tetrahedrization of its vertices, we use the iso-surface definition suggested in [17]. This definition has several interesting properties. It has also been extended to arbitrary dimensions in [18]. It is based, on one hand, on the digital connectedness of voxels and, on the other hand, on the location of the C-vertices on the grid.

In order that the paper be self-contained, we first briefly recall some definitions of digital and combinatorial topology (more general definitions can respectively be found in [16] and [1]). After that, we show how to construct iso-surfaces locally, 8-cubes by 8-cubes. In Section 2.3, we demonstrate that our iso-surfaces have the property to be included in the Delaunay tetrahedrization of their vertices.

2.2.1. Preliminary definitions

Definition 1 (6-, 18- and 26-adjacent voxels). Two voxels are said to be *6-adjacent* if their coordinates differ of ± 1 on exactly one coordinate. They are *18-adjacent* (respectively *26-adjacent*) if their coordinates differ of ± 1 on one or two coordinates (respectively one, two or three coordinates).

Definition 2 (6-, 18- and 26-connectedness). Let A be a subset of $\mathbb{Z}^3$. Two voxels a, $b \in A$ are *ρ-connected* in A (for $\rho \in \{6, 18, 26\}$) if there exists a sequence of voxels of A, starting with a and ending with b, such that two successive voxels are ρ-adjacent. The transitive closure of this relation is the *ρ-connectedness*, which defines *ρ-components* in A.

In the following, a κ-connectedness is associated with the inner voxels, and a λ-connectedness is associated with the outer voxels of $\mathcal{I}$. The pair (κ, λ) is called a *connectedness pair*.

Definition 3 (Combinatorial manifold [12,14]). A *2D combinatorial manifold* (*without boundary*) is a pair (G, F), where G is a graph and F is a set of loops over G with the following properties:

(i) every arc of G is adjacent to exactly two loops,
(ii) for any vertex u, the set of loops incident to u can be arranged into a circular permutation $(f_0, \ldots, f_{k-1})$, $k > 1$, called the *umbrella* of u, such that f_i is adjacent to f_{i+1} for any i, indices taken modulo k, and
(iii) any vertex u of G is incident to at least three arcs. A combinatorial manifold is said to be triangulated if all loops have size 3.

Definition 4 (2-manifold in $\mathbb{R}^3$ [1]). A *2-manifold* (*without boundary*) in $\mathbb{R}^3$ is a subset of $\mathbb{R}^3$ for which every point has a neighbourhood that is topologically equivalent to an open disk.

The topology of any 2-manifold in $\mathbb{R}^3$ can be represented by a combinatorial manifold. The converse is not true: not every 2D combinatorial manifold can be embedded in $\mathbb{R}^3$ as a 2-manifold (for instance, the Klein bottle). By definition, a 2-manifold has no self-intersection. Closed 2-manifolds in $\mathbb{R}^3$ are orientable [1].

Definition 5. A surface S is said to be an ε-approximation of the surface S_0, if for any point $m \in S$, there exists a point $m_0 \in S_0$ such that $d(m, m_0) < \varepsilon$.

2.2.2. $\kappa\lambda$-iso-surface construction

In this section, we first construct a triangulated approximation of the iso-surface of level C, as a 2D combinatorial manifold without boundary. Since the construction depends on the connectedness pair (κ, λ), we call the result a $\kappa\lambda$-iso-surface. We enforce $\kappa\lambda$-iso-surfaces to be identical to $\lambda\kappa$-iso-surfaces of the negative image of $\mathcal{I}$. It has been shown in [17] that this condition implies (κ, λ) is one of $(6, 18)$, $(6, 26)$, $(18, 6)$ and $(26, 6)$. Therefore, we will only examine the connectedness pairs $(18, 6)$ and $(26, 6)$. For a more complete description of the construction of $\kappa\lambda$-iso-surfaces, please refer to [17].

Following the MC principle, $\kappa\lambda$-iso-surfaces are built locally, 8-cubes by 8-cubes. Any voxel of the image is embedded into $\mathbb{R}^3$ as a point. Each 8-cube is embedded into $\mathbb{R}^3$ as a cube whose vertices are the embeddings of the eight voxels of the 8-cube.

Let H be an 8-cube of $\mathcal{I}$. Let $I = \{i_1, \ldots, i_l\}$ be the set of inner voxels of H and $E = \{e_1, \ldots, e_k\}$ be the set of its C-vertices. For $\kappa = 26$, I is always κ-connected. For $\kappa = 18$, I is κ-connected except for four configurations: the configurations with two diagonally opposite inner voxels (say i_1 and i_2) and six outer voxels (which induce two κ-components). These four configurations are called *disconnected*. All other configurations are called *connected*. For any connected configuration, the *local C-convex hull* of H is defined as $\mathrm{Hull}(E \cup I)$. For any disconnected configuration, the inner voxel i_1 (respectively i_2) is bordered by a set of three C-vertices E_1 (respectively E_2); the *local C-convex hull* of H is then defined as $\mathrm{Hull}(E_1 \cup i_1) \cup \mathrm{Hull}(E_2 \cup i_2)$.

The *C-edges* of H are defined as the edges of the local C-convex hull of H that connect two C-vertices. These C-edges belongs by definition to the boundary of the local C-convex hull of H. Let $\mathcal{H}$ be the embedding of H into $\mathbb{R}^3$ (i.e., a cube). The C-edges of H that lie on $\partial\mathcal{H}$ are called *bordering C-edges*, the other ones are called *inside C-edges*. The bordering C-edges of any configuration can be arranged into a set of loops, that are called *C-loops*. Fig. 1 displays all the possible configurations and the corresponding C-edges and C-loops. As illustrated by Fig. 2, C-edges depend both on the connectedness pair $\{\kappa, \lambda\}$ and on the geometry of the C-vertices. However, the bordering C-edges and, consequently, the amount and

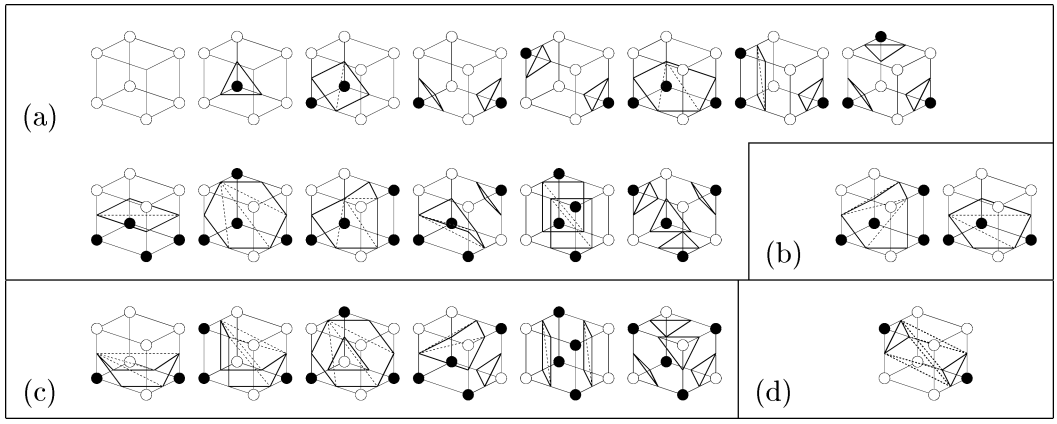

Fig. 1. C-loops created for classical configurations and triangulation of these loops. C-loops over bordering C-edges are displayed as solid thick lines, inside C-edges as dashed thick lines. The connectedness pair has an influence on both the construction of the C-loops and their triangulation: (a) C-loops and C-edges created for $(\kappa, \lambda) \in \{(6, 18), (6, 26)\}$; (b) when $(\kappa, \lambda) \in \{(18, 6), (26, 6)\}$, these configurations have the same C-loops than in (a), but different inside C-edges; (c) when $(\kappa, \lambda) \in \{(18, 6), (26, 6)\}$, these configurations have different C-loops than in (a); (d) special case when $(\kappa, \lambda) \equiv (26, 6)$ (a symmetric case exists when $(\kappa, \lambda) \equiv (6, 26)$).

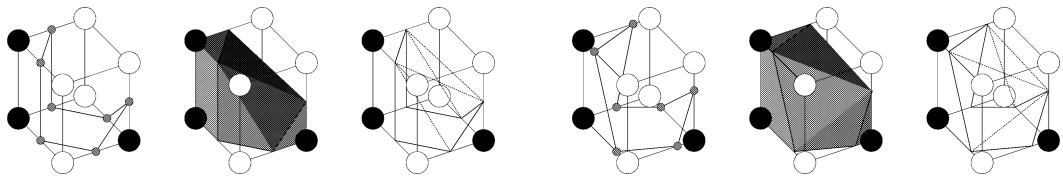

Fig. 2. Depending on the location of C-vertices, the $\kappa\lambda$-iso-surface built locally inside a given 8-cube may change. From left to right, C-loops built on C-vertices, C-convex hulls and C-edges ($(\kappa, \lambda) \in \{(18, 6), (26, 6)\}$).

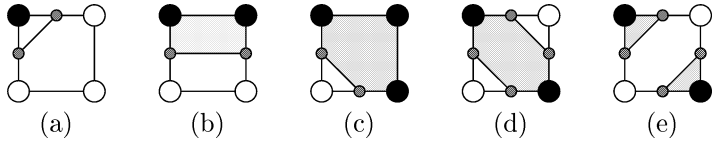

Fig. 3. The figure displays the bordering C-edges that are built on the faces of 8-cubes according to the classification ("inner" or "outer") of their voxels. For cases (a), (b) and (c) the construction is independent of $\{\kappa, \lambda\}$. The case (d) occurs when $\lambda = 6$ and $\kappa \in \{18, 26\}$. The case (e) occurs when $\kappa = 6$ and $\lambda \in \{18, 26\}$.

the length of C-loops, are independent of the geometry of the C-vertices. The following theorem shows that the C-vertices, the C-edges and the C-loops form a combinatorial surface.

Theorem 6. *Let G be the graph whose vertices* (*respectively arcs*) *are the C-vertices* (*respectively the bordering C-edges*) *of all the* 8*-cubes of the image. The graph G together with the loops defined over the arcs of G by the C-loops is a* 2*D combinatorial manifold without boundary. Moreover, it is triangulated by the inside C-edges. The resulting set is a triangulated* 2*D combinatorial manifold without boundary denoted by T.*

Proof. Since the image $\mathcal{I}$ is finite and its border is composed of only inner voxels or only outer voxels, every bordering C-edges belongs to two adjacent 8-cubes. As shown by Figs. 3 and 1, the bordering C-edges defined on one 8-cube are identical to the bordering C-edges defined on the adjacent 8-cube. Moreover, within each 8-cube, every bordering C-edge belongs to exactly one C-loop. Thus, every arc of G is adjacent to exactly two loops. Now, let c be a C-vertex. The point c belongs to four 8-cubes. Within each 8-cube, the point c belongs to one C-loop (see Fig. 1). If we consider the four 8-cubes around c we can arrange the four loops into an umbrella. Since c has four incident arcs, the first statement holds. Fig. 1 also shows that, whichever is the 8-cube configuration, the C-loops are triangulated by the inside C-edges, which concludes the argument. □

Finally, we define the $\kappa\lambda$-iso-surface of level C as the embedding of C-loops, triangulated by C-edges.

Theorem 7. *The $\kappa\lambda$-iso-surface of level C is a* 2*-manifold without boundary in $\mathbb{R}^3$.*

Proof. The $\kappa\lambda$-iso-surface of level C is defined as the embedding of T in $\mathbb{R}^3$. The loops of T have length 3. Every loop can be embedded as an open triangle between the C-edges that define it. Let M be the subset of subsets of $\mathbb{R}^3$ composed of the C-vertices, the open C-edges, and those open triangles. Within each 8-cube, it is clear that these elements are pairwise disjoint (as defined over the local C-convex hull). Now, two elements of M that belong to two different 8-cubes cannot intersect by construction. As a consequence, all the elements of M are pairwise disjoint and M forms a *triangulation* (e.g., see [1]). The embedding of M into $\mathbb{R}^3$ is the subset of $\mathbb{R}^3$ composed of the union in $\mathbb{R}^3$ of all the elements of M (sometimes called the *body* of M). Since T is a 2D combinatorial manifold without boundary, the embedding of M into $\mathbb{R}^3$ is a 2-manifold without boundary. □

Theorem 8. *The $\kappa\lambda$-iso-surface of level C separates κ-components of inner voxels from λ-components of outer voxels.*

Proof. (A complete proof can be found in [18, Theorem 22].) There is no segment linking two κ-adjacent inner voxels which intersects the $\kappa\lambda$-iso-surface of level C. The same holds for λ-adjacent outer voxels. Now, each component of the $\kappa\lambda$-iso-surface is a connected 2-manifold in $\mathbb{R}^3$. The Jordan–Brouwer theorem (e.g., see [1]) concludes the argument. □

Let r be the maximum distance between two 6-adjacent voxels of $\mathcal{I}$. The finer is the sampling, the smaller is r and the better is the $\kappa\lambda$-iso-surface approximation of $\mathcal{S}_C$.

Theorem 9. *The $\kappa\lambda$-iso-surface of level C is a $\sqrt{3}r$-approximation of the surface $\mathcal{S}_C$.*

Proof. Let e be any C-vertex of the $\kappa\lambda$-iso-surface of level C. The vertex e lies between two voxels a and b such that either $h(a) \geqslant C$ and $h(b) < C$ or $h(a) < C$ and $h(b) \geqslant C$. Since h is continuous, there must be a point m of the segment $[ab]$ with $h(m) = C$. It is obvious that $\|m - e\| \leqslant r$. We have just shown that any C-vertex of the $\kappa\lambda$-iso-surface of level C is at most at a distance r of $\mathcal{S}_C$. If we increase the sampling density by a given factor, all the vertices of the $\kappa\lambda$-iso-surface come closer to $\mathcal{S}_C$ with the same factor. We conclude the argument since every triangle of the $\kappa\lambda$-iso-surface is defined locally and has a size no greater than $\sqrt{3}r$. □

We have just exhibited a method to construct locally an iso-surface of level C in an image $\mathcal{I}$. This construction is performed 8-cube by 8-cube. Unlike the MC algorithm, the inside C-edges are dependent on the geometry of the neighboring C-vertices: the precomputation of a table of 256 configurations is not sufficient to extract the pieces of surface within one 8-cube. However, a careful case study has shown that this task can be performed very efficiently [3].

2.3. Inclusion in the Delaunay graph

We will now prove that an iso-surface built as described above has the interesting property to be included in the Delaunay tetrahedrization of its vertices. To establish this result, we first show that Delaunay edges built inside an 8-cube do not depend on C-vertices located outside this 8-cube. In the following, S_C designates a $\kappa\lambda$-iso-surface of level C in the image $\mathcal{I}$, which is computed as described above, and V_C is the set of its vertices.

Theorem 10. *Let $\{e_1, e_2, \ldots, e_k\}$ be the k C-vertices of a given 8-cube. Then*

$$\partial\mathrm{Hull}\big(\{e_i\}_{i=1,\ldots,k}\big) \subset \mathrm{Del}\big(\{e_i\}_{i=1,\ldots,k}\big) \subset \mathrm{Del}(V_C).$$

Proof. The first inclusion is immediate. To prove the second inclusion, we compute the intersection of the smallest sphere B enclosing e_i and e_j with the discrete grid. This computation can be achieved by simple geometrical considerations: we use the fact that for any point v on the sphere B, the straight-lines (ve_i) and (ve_j) are orthogonal. Let P be the smallest straight parallelepiped enclosing e_i and e_j. The vertices of P are located on the sphere B. As P remains inside the considered 8-cube (see Fig. 4), the sphere B does not intersect grid edges of other 8-cubes. Consequently, the sphere B contains no points from $E \setminus \{e_1, e_2, \ldots, e_k\}$ in its interior, which implies the second inclusion. □

Theorem 11. $S_C \subset \mathrm{Del}(V_C)$.

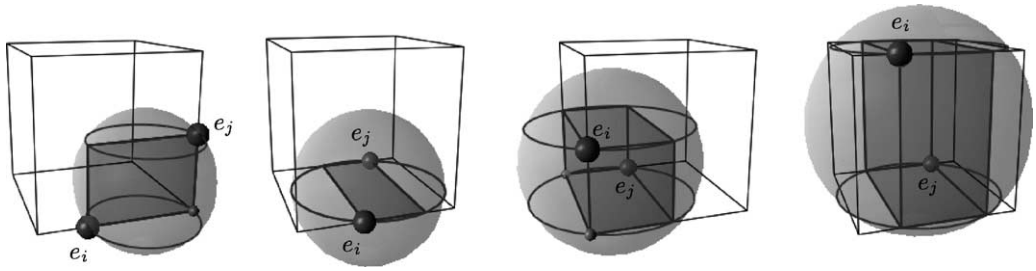

Fig. 4. To examine the intersection of the sphere B with diameter $[e_i e_j]$, four different cases must be considered, which correspond to different positions of the C-vertices e_i and e_j on the 8-cube. The smallest parallelepiped P enclosing e_i and e_j has been drawn. It always lies inside the 8-cube. To understand how the sphere intersects the discrete grid, the circles corresponding to the intersections of the sphere with horizontal planes passing through a and b have also been drawn. Those circles do not intersect edges from other 8-cubes.

Proof. Each edge $[ee']$ of S_C is a C-edge of some 8-cube H. Two cases arise: either H forms a connected configuration in $\mathcal{I}$ or H forms a disconnected configuration. Assume first that H is a connected configuration. Let I be the inner voxels of H and E be the set of C-vertices of H. Then $[ee']$ is an edge of the local C-convex hull of H, i.e., $[ee']$ is an edge of $\partial\text{Hull}(I \cup E)$. This implies that both e and e' are extremal points of $\text{Hull}(I \cup E)$. Since e and e' belong to E, they are also extremal points of $\text{Hull}(E)$. The segment $[ee']$ being an edge of $\text{Hull}(I \cup E)$, it must be an edge of $\text{Hull}(E)$. We get $[ee'] \subset \partial\text{Hull}(E)$. Theorem 10 induces $[ee'] \subset \text{Del}(V_C)$. The case where H forms a disconnected configuration can be proven similarly. Since every edge of S_C belongs to $\text{Del}(V_C)$, every triangle of S_C belongs to $\text{Del}(V_C)$. This concludes the argument. □

3. Skeleton extraction from iso-surfaces

3.1. Computation

In this section, iso-surfaces are applied to the computation of the skeleton of objects. By definition, the skeleton $\text{Sk}(X)$ of an object X is the locus of the centers of the maximal balls of X. A ball B included in X is said to be maximal if there exists no other ball included in X and containing B (Fig. 5).

Numerous methods have been proposed to extract the skeleton. They can be classified in two main families: *discrete methods* and *continuous methods*. Discrete methods work directly on binary images. The skeleton is a set of pixels that is computed using distance transforms [8,27] or morphological thinnings [19,20,22,23]. Continuous methods are generally based on the Voronoi graph of a set of points located on the boundary of the object [4,7,9,24].

In this paper, we focus on the second family of methods. We use the approach proposed by Boissonnat [5]. The input is a triangulated surface S which approaches the boundary of the object X. Let V be the set of vertices of S. If the surface S is included in the Delaunay tetrahedrization $\text{Del}(V)$, there are exactly two distinct types of Delaunay tetrahedra: *inner tetrahedra* lying inside S and *outer tetrahedra* lying outside S. The skeleton is defined as a subset of the Voronoi diagram. This subset is the dual of the inner Delaunay elements. The skeleton is a set of Voronoi polygons, edges and vertices making pieces of surfaces in 3D. This method works only if the surface S is included in the Delaunay tetrahedrization

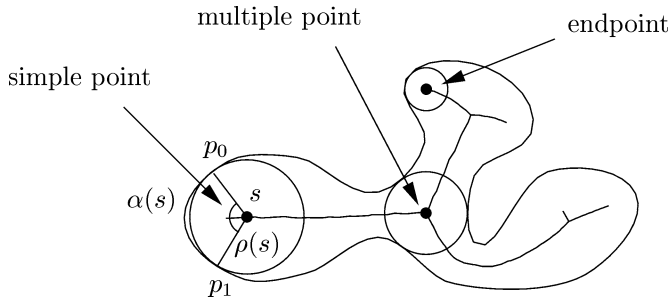

Fig. 5. Terminology relative to skeletons.

of its vertices Del(V). The iso-surfaces constructed in the previous part satisfy this condition and can therefore be used to compute the skeleton.

Depending on the choice of inner and outer connectedness, different types of $\kappa\lambda$-iso-surfaces can be generated for the same volumetric data and the same threshold C. We use the connectedness pair (6, 18) in order to minimize the amount of loops in the object. This improves the efficiency of the filtering step.

3.2. Filtering

Iso-surfaces extracted from volumetric images may happen to be slightly noisy. In particular, noise originates from the quantification step, as gray-levels take a finite number of values ranging from 0 to 255. We will consider that sample points are not located exactly on the boundary of the object but have the form $p_i + e_i$ where p_i belongs to the boundary of the real object and e_i is a "small" vector representing the perturbation of the point p_i around the boundary.

Even if negligible compared to the size of voxels, presence of noise on sample points may lead to a radical change in the skeleton. For instance, in the case of a sphere, the shift of one sample point towards the center of the sphere will change the whole Delaunay tetrahedrization, leading to a completely different approximated skeleton. Indeed, the shifted point will become the Delaunay neighbor of every other points.

A filtering step is therefore necessary to remove peripheral branches associated to nonsignificant parts of the object. In order to preserve the skeleton homotopy type, the filtering step removes the skeleton points located on the border of the skeleton. Different removing criteria have been proposed in the literature. One can for instance measure the difference between the initial shape and the shape reconstructed from the simplified skeleton. Branches are shortened as long as this difference remains smaller than a fixed threshold [9]. More complex criteria may be found in [24].

In the following, we will distinguish three types of skeleton points: *simple points* whose maximal sphere touches the object boundary on two contact points, *endpoints* whose maximal sphere touches the object boundary on one point and *multiple points* whose maximal sphere touches the boundary on at least three contact points. Our filtering criterion is based on the two following notions (Fig. 5).

Definition 12 (Thickness). The thickness $\rho(s)$ at a point s of the skeleton is the radius of the maximal ball centered on s.

Definition 13 (Bisector angle [28]). Let s be a skeleton point. If s is a simple point, let a and b be the two contact points of the maximal ball centered on s. The bisector angle $\alpha(s)$ is the angle $\widehat{asb}$ lying between 0 and π. If s is an endpoint, $\alpha(s) = 0$. If s is a multiple point, $\alpha(s) = \max(\widehat{asb})$, where a and b are any two contact points of the maximal ball centered at s.

Thickness and bisector angle can both be defined in Euclidean spaces of arbitrary dimension. The thickness function is continuous. The bisector angle function is continuous except at multiple points. The thickness is extremum where the bisector angle equals π and the thickness equals 0 at endpoints of the skeleton.

In practice, the skeleton is approximated with the Voronoi graph of sample points. Therefore, thickness and bisector angle need to be approximated as well. We restrict our computation to the Voronoi vertices as they provide a dense sampling of the skeleton. Let s designates a Voronoi vertex of the approximated skeleton and $[p_0p_1p_2p_3]$ its associated Delaunay tetrahedron. The thickness $\rho(s)$ and the bisector angle $\alpha(s)$ are approximated as follows:

$$\begin{aligned}\rho(s) &= d(s, p_0) = d(s, p_1) = d(s, p_2) = d(s, p_3),\\ \alpha(s) &= \max_{i\neq j}(\widehat{p_isp_j}).\end{aligned}$$

Indeed, the sphere passing through the four points p_0, p_1, p_2, p_3 approximates a maximal ball. In the most general case, s approaches a simple point of the skeleton and the maximal ball intersects the boundary at two contact points a and b. Therefore, the four points p_0, p_1, p_2, p_3 tend either to the contact point a or to the contact point b. The angle $\widehat{p_isp_j}$ between any two points p_i and p_j is either close to 0 or close to the bisector angle. By taking the maximum of $\widehat{p_isp_j}$, we get an approximation of the bisector angle.

In order to visualize the effect of noise, one can represent the vertices s of the skeleton on a graph entitled the *parameter graph* in which vertices are plotted according to $\rho(s)$ against $\alpha(s)$ instead of their classical Cartesian coordinates. Thus, each vertex s of the skeleton is associated with a point having coordinates $(\alpha(s), \rho(s))$ in the parameter graph.

When there is no noise (synthetic object of Fig. 6(a)–(c)), the skeleton structures are easily identified within the parameter graph. Endpoints lie on the straight-line ($\alpha = 0$) and branches are represented by curves, reflecting the continuity of the thickness and the bisector angle.

When noise is added to the shape boundary (Fig. 6(d)–(f)), the aspect of the parameter graph changes. Indeed, most of the vertices that were initially lying on the branches of the skeleton are now scattered next to the bottom left of the parameter graph. They plot an hyperbolic-like form.

The same phenomenon occurs with objects obtained from binary images. However, in the latter case, points organize themselves in parallel strata (Fig. 6(g)–(i)).

It is possible to explain that the noise induces an hyperbolic-like form. Let s be a vertex of the skeleton, a and b the two points of the boundary such that $\alpha(s) = \widehat{asb}$ and $\rho(s) = d(a, s) = d(b, s)$. The set of vertices s generated by two boundary points a and b at distance l from each other can be described by the equation

$$\rho = \frac{l}{2\sin(\alpha/2)}.$$

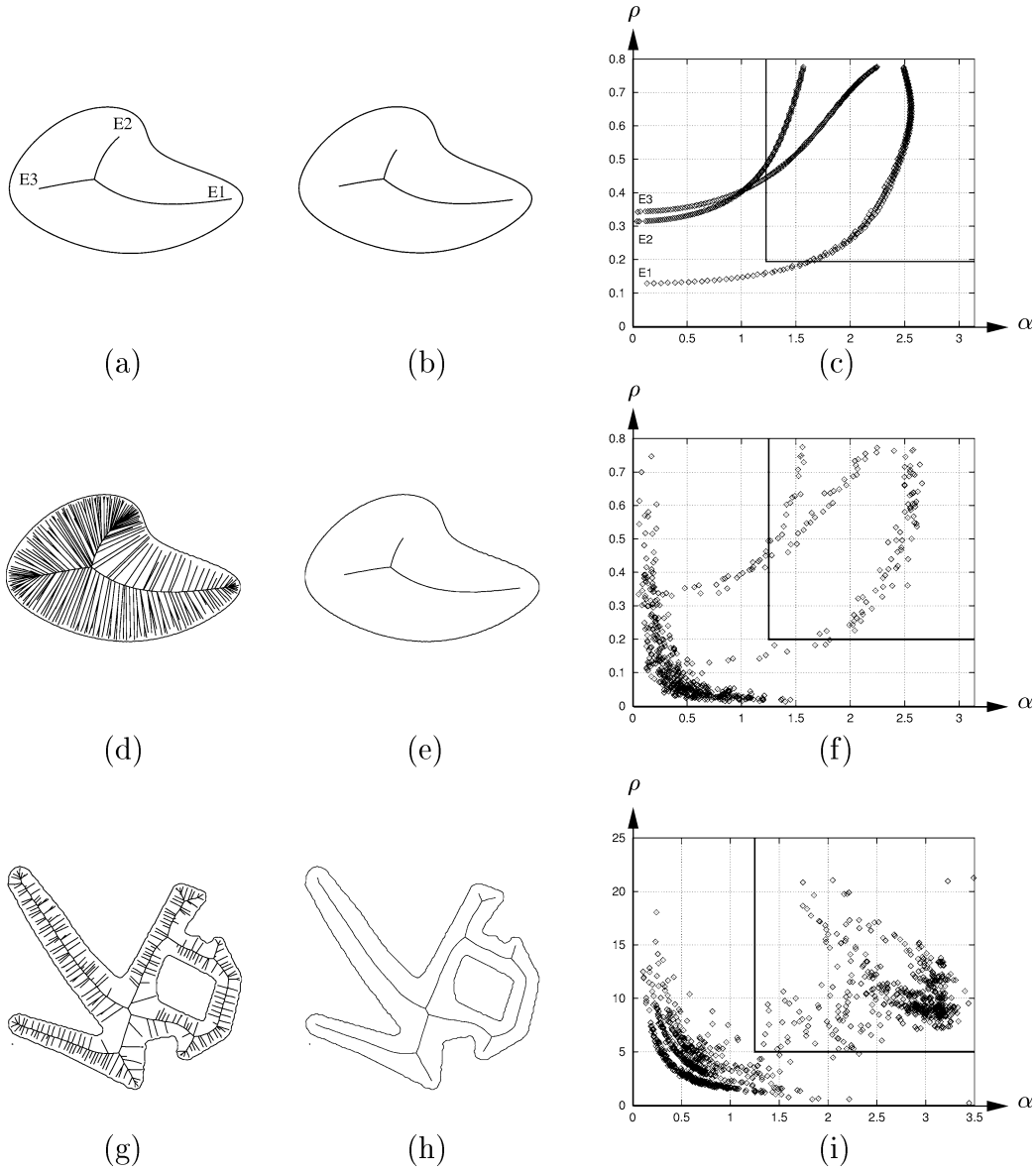

Fig. 6. (a,d,g) Skeleton of a synthetic object, of the same object after a slight perturbation of sample points on the boundary, and of an object extracted from a binary image. (b,e,h) Simplified skeletons. (c,f,i) Parameter graphs and thresholds chosen for filtering.

If one plots ρ as a function of α with a fixed value for l on the parameter graph, a curve is obtained which perfectly fits the hyperbolic-like form (Fig. 7). With objects obtained from binary images, the distance l between two boundary points is quantified (owing to the discrete representation of binary images and the half-integer values of the sample point coordinates). This is confirmed by the presence of strata in the noise hyperbolic-like form.

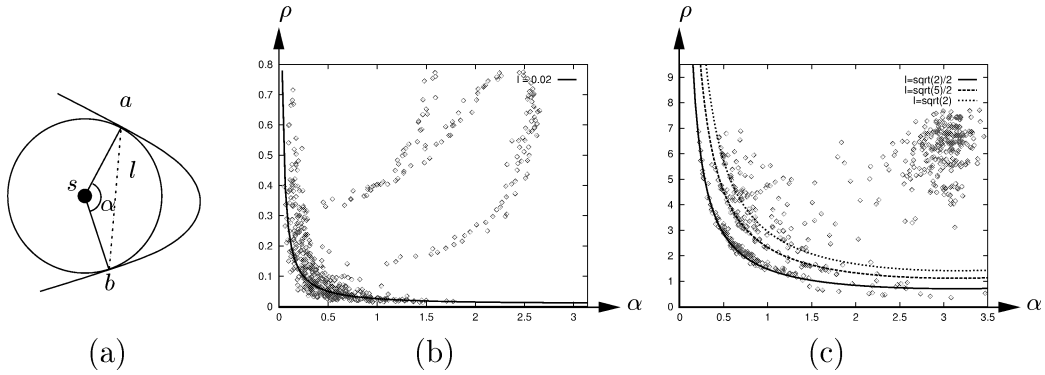

Fig. 7. Modeling noise with $\rho = l/(2\sin(\alpha/2))$.

Consequently, the noise disturbs neighbourhood relationships in the Voronoi graph. Boundary points at distance l from each other generate parasite branches on the skeleton. When noise remains small, l is also small. Perturbations due to noise stay local.

The previous discussion shows that noisy vertices of the skeleton are characterized by a small bisector angle or a small thickness. Consequently, we propose to remove an endpoint s of the current skeleton if the two parameters $\alpha(s)$ and $\rho(s)$ satisfy

$$(\alpha(s) < \alpha_0) \quad \text{or} \quad (\rho(s) < \rho_0).$$

The proposed criterion depends on two thresholds α_0 and ρ_0. The first one, α_0 controls the lost of information. If α_0 equals 0, the skeleton is never simplified. The second threshold ρ_0 gives an indication of the object size. The two thresholds can be selected directly on the parameter graph. Indeed, in this representation, our simplification method consists in removing progressively endpoints located below the thick polygonal line plotted on the parameter graphs (Fig. 6). This polygonal line cuts off the hyperbolic-like form from the rest of the graph.

The hyperbolic-like form of noise on the parameter graph suggests that a better filtering would be obtained with the hyperbolic line $\rho = l/(2\sin(\alpha/2))$. However, this approach did not give convincing results. By doing so, the filtering depends on the unique parameter l, against two independent parameters ρ_0 and α_0 before. As a consequence, the filtering parameterization is less flexible.

4. Results and applications

Some results on volumetric images are presented in Fig. 8. The first two volumes were generated synthetically and correspond respectively to the discretization of a parallelepiped and an ellipsoid. As expected, the skeleton computation provides pieces of planes and an ellipse. The second and third volumes are real images corresponding respectively to a bone sample and a human heart. The volume sizes are $30 \times 30 \times 30$ and $85 \times 85 \times 98$. The amount of vertices on each iso-surface is 5822, 2376, 3272 and 36640, respectively. The running time for computing both the iso-surface and the skeleton was respectively 23, 3, 6 and 115 seconds on an SGI O2 R4000. We emphasize that the surface portions making the skeleton have a smooth aspect. Such a smooth aspect is particularly tricky to achieve with purely discrete approaches.

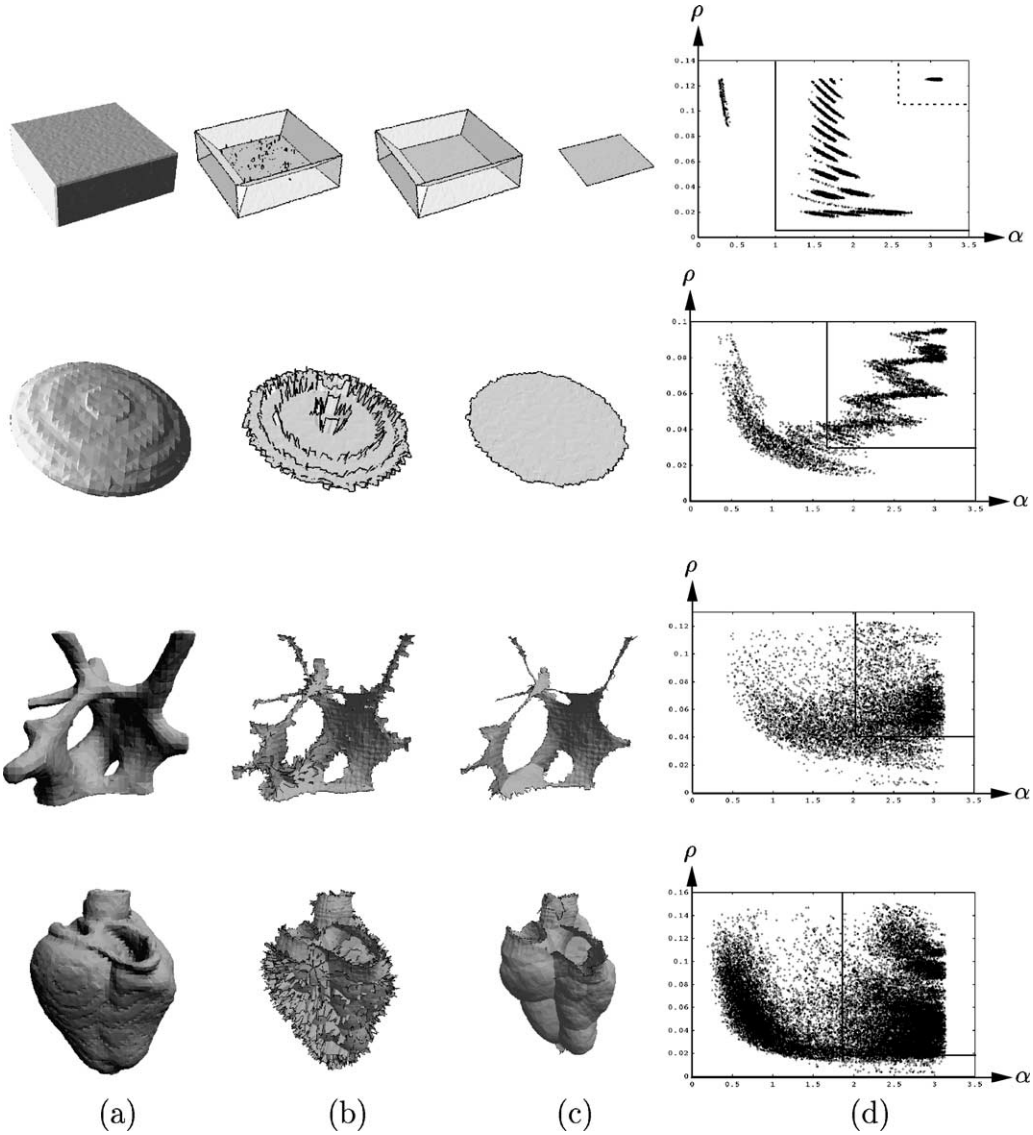

Fig. 8. (a) Delaunay conforming iso-surfaces. (b) Skeletons extracted from iso-surfaces. (c) Skeletons after filtering. (d) Parameter graphs. Two different thresholds have been applied on the first iso-surface (the box). It shows the influence of the different parts of the parameter graph.

In many applications, the thickness of an object is an important characteristic feature. In the previous section, thickness has been defined at any point of the skeleton. It is interesting to extend this definition at any point m on the boundary of the object. We define the thickness at m as the radius of the maximal ball passing through m. Some results are presented in Fig. 9. The thickness has been computed after simplification of the skeleton. One can for instance notice a difference of thickness between the two heart ventricles. The thickness is maximal at the branching point of the bone sample.

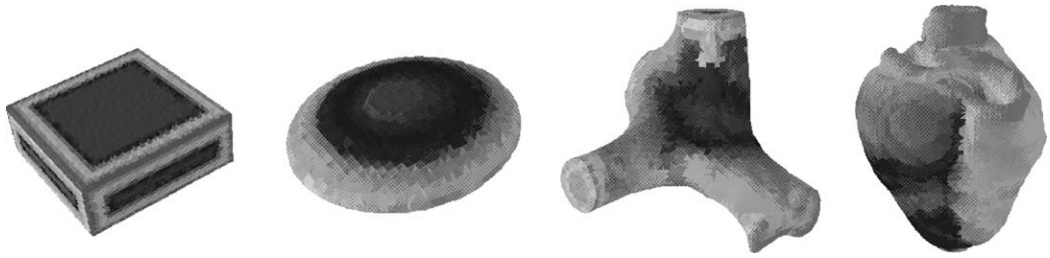

Fig. 9. Computation of thickness on the object boundary.

5. Conclusion

In this paper, we have constructed a new type of iso-surfaces: they are 2-manifolds without boundary in $\mathbb{R}^3$ and they are included in the Delaunay graph of their vertices. The proof uses simple geometrical considerations and holds, whatever is the voxel size. The Voronoi diagram is used to compute the skeleton of these iso-surfaces. We analyze the influence of noise on the skeleton. We deduce a characterization of noisy branches and a simplification method for continuous skeletons. Future work includes the use of the skeleton to extract parameters and segment objects. It would also be interesting to verify that $\kappa\lambda$-iso-surfaces are Delaunay conforming for arbitrary dimension, since their definition is not restricted to $\mathbb{R}^3$.

Acknowledgements

Our deepest thanks to Francoise Peyrin for the bone sample volume and to Yves Usson for the heart volume. The bone sample was acquired at the European Synchrotron Radiation Facility (ESRF) by computed microtomography [25]. The heart data was obtained with a polarized light optical bench [15].

References

[1] P.S. Aleksandrov, Combinatorial Topology, Graylock Press, Baltimore, MD, 1960.
[2] N. Amenta, M. Bern, Surface reconstruction by Voronoi filtering, Discrete Comput. Geom. 22 (4) (1999) 481–504.
[3] D. Attali, J.-O. Lachaud, Constructing iso-surfaces satisfying the Delaunay constraint; application to the skeleton computation, in: Proc. 10th Int. Conf. on Image Analysis and Processing (ICIAP'99), Venice, Italy, 27–29 September 1999, pp. 382–387.
[4] D. Attali, A. Montanvert, Semicontinuous skeletons of 2d and 3d shapes, Comput. Vision Image Understanding 67 (3) (1997) 261–273.
[5] J.D. Boissonnat, Shape reconstruction from planar cross sections, Comput. Vision Graph Image Process. 44 (1988) 1–29.
[6] J.-D. Boissonnat, F. Cazals, Smooth surface reconstruction via natural neighbor interpolation of distance functions, in: Proc. 16th Annu. ACM Sympos. Comput. Geom., 2000.
[7] J.D. Boissonnat, B. Geiger, Three dimensional reconstruction of complex shapes based on the Delaunay triangulation, Technical Report No. 1697, INRIA, May 1992.

[8] G. Borgefors, Centres of maximal disks in the 5-7-11 distance transform, in: 8th Scandinavian Conf. on Image Analysis, Tromsø, Norway, 1993, pp. 105–111.
[9] J.W. Brandt, V.R. Algazi, Continuous skeleton computation by Voronoi diagram, CVGIP: Image Understanding 55 (3) (1992) 329–337.
[10] L.P. Chew, Guaranteed-quality mesh generation for curved surfaces, in: Proc. 9th Ann. Sympos. on Comput. Geom., 1993, pp. 274–280.
[11] H. Edelsbrunner, E.P. Mücke, Three-dimensional alpha shapes, ACM Trans. Graphics 13 (l) (1994) 43–72.
[12] J. Françon, Discrete combinatorial surfaces, CVGIP: Graphical Models Image Process. 57 (l) (1995) 20–26.
[13] A. Van Gelder, J. Wilhelms, Topological considerations in isosurface generation, ACM Trans. Graphics 13 (4) (1994) 337–375.
[14] M. Henle, A Combinatorial Introduction to Topology, Dover, New York, 1994.
[15] P.-S. Jouk, Y. Usson, G. Michalowicz, F. Parazza, Mapping of the orientation of myocardial cells by means of polarized light confocal scanning laser microscopy, Microscopy Res. Technique 30 (1995) 480–490.
[16] T.Y. Kong, A. Rosenfeld, Digital topology: Introduction and survey, Comput. Vision Graphics Image Process. 48 (3) (1989) 357–393.
[17] J.-O. Lachaud, Topologically defined iso-surfaces, in: 6th Discrete Geometry for Computer Imagery, Lyon, France, Lecture Notes in Computer Science, Vol. 1176, Springer, 1996, pp. 245–256.
[18] J.-O. Lachaud, A. Montanvert, Continuous analogs of digital boundaries: A topological approach to iso-surfaces, Graphical Models Image Process. 62 (2000) 129–164.
[19] L. Lam, S.-W. Lee, C.Y. Suen, Thinning methodologies – a comprehensive survey, IEEE Trans. PAMI 14 (9) (1992) 869–885.
[20] T. Lee, R.L. Rangasami, Building skeleton models via 3-d medial surface/axis thinning algorithms, CVGIP: Graphical Models Image Process. 56 (6) (1994) 462–478.
[21] W.E. Lorensen, H.E. Cline, Marching cubes: A high resolution 3D surface construction algorithm, Comput. Graphics 21 (4) (1987) 163–169.
[22] G. Malandain, G. Bertrand, Fast characterization of 3D simple points, in: 11th ICPR, 1992, pp. 232–235.
[23] S. Miguet, V. Marion-Poty, A new 2-D and 3-D thinning algorithm based on successive border generations, in: 4th Discrete Geometry for Computer Imagery, Grenoble, 1994, pp. 195–206.
[24] R. Ogniewicz, A multiscale MAT from Voronoi diagrams: the skeleton-space and its application to shape description and decomposition, in: C. Arcelli et al. (Eds.), Aspects of Visual Form Processing, World Scientific, Singapore, 1994, pp. 430–439.
[25] F. Peyrin, M. Pateyron, A.M. Laval-Jeantet, P. Cloetens, Analysis of bone micro-architecture from high resolution 3d synchrotron radiation microtomography images, in: 10th Conference of the European Society of Biochemistry, Louvain, Belgium, 1996, p. 211.
[26] J.R. Shewchuk, Tetrahedral mesh generation by Delaunay refinement, in: Proc. 14th Ann. Sympos. on Comput. Geom., 1998, pp. 86–95.
[27] E. Thiel, Les distances de chanfrein en analyse d'images: Fondements et applications, Ph.D. Thesis, Université Joseph Fourier, Grenoble I, 1994.
[28] L. Vincent, Efficient Computation of Various Types of Skeletons, SPIE's Medical Imaging V, Vol. 1445, SPIE, San Jose, CA, 1991.